



OPEN

Vibrational disorder and densification-induced homogenization of local elasticity in silicate glasses

Omar Benzine¹, Zhiwen Pan¹, Courtney Calahoo¹, Michal Bockowski², Morten M. Smedskjaer³, Walter Schirmacher⁴ & Lothar Wondraczek¹✉

We report the effect of structural compaction on the statistics of elastic disorder in a silicate glass, using heterogeneous elasticity theory with the coherent potential approximation (HET-CPA) and a log-normal distribution of the spatial fluctuations of the shear modulus. The object of our study, a soda lime magnesia silicate glass, is compacted by hot-compression up to 2 GPa (corresponding to a permanent densification of ~ 5%). Using THz vibrational spectroscopic data and bulk mechanical properties as inputs, HET-CPA evaluates the degree of disorder in terms of the length-scale of elastic fluctuations and the non-affine part of the shear modulus. Permanent densification decreases the extent of non-affine elasticity, resulting in a more homogeneous distribution of strain energy, while also decreasing the correlation length of elastic heterogeneity. Complementary ²⁹Si magic angle spinning NMR spectroscopic data provide a short-range rationale for the effect of compression on glass structure in terms of a narrowing of the Si–O–Si bond-angle and the Si–Si distance.

Elasticity is a primary design target in modern glass science and technology^{1,2}. For a variety of applications, it is often desirable to adapt glass formulations for enhanced shear and/or Young's modulus and, thus, enhanced rigidity or stiffness³. For example, this may enable reduction of the wall thickness of a glass product in a given application and, hence, reduction of product weight and embodied CO₂. To this end, the effect of glass composition on elastic moduli is often estimated to a satisfactory accuracy using semi-empirical mixing or regression models^{4–9}. Most of these approaches start from the Makishima-Mackenzie (MM) model⁵, which remains today's most popular approach for predicting Young's modulus from a glass composition. It takes into account the dissociation energies of the oxide constituents in crystalline form, and the corresponding occupied volume as derived from ionic radii. However, the MM model as well as follow-up approaches are known to frequently underestimate^{3,10,11} or overestimate¹² Young's modulus. As often pointed-out, MM-type approaches perform best only for glasses with compositions close to a corresponding crystal of equivalent density, for which the ionic radii are precisely known³. Deviations from such model descriptions are due to disorder-related local variations of the structural cohesion¹³.

The existence of spatially heterogeneous elasticity is well established through in silico^{14,15} and experimental^{16,17} studies of simple glasses. 'Soft' and 'hard' domains were found to coexist across a typical length scale of a few nanometers (or a few tens of particles^{18,19}). This heterogeneous nature is reflected in the observation that displacement fields on the microscopic level differ from macroscopic strain analysis, what has been described as *non-affine* displacement^{20,21}. During non-affine deformation, individual particles undergo correlated displacements. The associated mesoscopic correlation length was found to be comparable to the one of elastic heterogeneity^{15,22}. In effect, this heterogeneous response leads to a significant decrease in the effective elastic moduli (as compared to a classical *affine* approximation such as the Born–Huang theory²³).

Several methods have been proposed to map the local elastic properties of simple model glasses, mostly by numerical simulation^{14,24}, but real-world experimental data remain difficult to obtain. Proposed methods are sometimes ambiguous in terms of the assessed length scale (e.g.,²⁵). An analytical framework for the evaluation of spatially fluctuating elastic constants is provided by the heterogeneous-elasticity theory (HET²⁶). HET

¹Otto Schott Institute of Materials Research, University of Jena, 07743 Jena, Germany. ²Institute of High-Pressure Physics, Polish Academy of Sciences, 01-142 Warsaw, Poland. ³Department of Chemistry and Bioscience, Aalborg University, 9220 Aalborg, Denmark. ⁴Institute of Physics, University of Mainz, 55099 Mainz, Germany. ✉email: lothar.wondraczek@uni-jena.de

assumes that spatial disorder leads to random fluctuations in structural rigidity. On this assumption, it provides expressions for the vibrational density of states and enables predictions of the frequency-dependence of Raman scattering and of the temperature-dependence of the heat capacity in disordered solids²⁷. In return, HET can be employed to quantify heterogeneous elasticity, non-affinity and the underlying length scales using experimental data such as Raman scattering spectra and/or low-temperature heat capacity for input²⁸. In the present paper, we follow this approach to elucidate the effects of network compaction on heterogeneous elasticity in the archetypal soda-lime-magnesia silicate (SLMS) glass. SLMS is representative for the most common group of glass materials used in commodity products such as glass containers, windows, tableware or automotive windshields. We use HET as a means to assess elastic disorder in SLMS and investigate variations in the population density distribution (PDD) of the local shear modulus $P(G)$ which occur as the fictive pressure of the glass increases to 2 GPa. From this, we extract pressure-induced changes in non-affine elasticity. The PDD is obtained from the coherent potential approximation of HET (HET-CPA) with THz Raman spectroscopic data for input. For a visual representation of the pressure-induced changes in elastic disorder, we then employ the obtained correlation length, the extent of non-affinity and the geometric mean of the analyzed shear modulus to construct a glass with corresponding shear modulus fluctuation *in silico*. On these models, we map the characteristic distribution of strain energy, which arguably reflects non-affinity in the real-world material. The observed relations are compared to short-range structural information using nuclear magnetic resonance spectroscopy as a complementary method.

Materials and methods

Sample material. *Sample synthesis.* The glass used in this study was prepared by conventional melt quenching from a batch of SiO_2 , MgCO_3 , CaCO_3 , and Na_2CO_3 to yield a glass composition of 70 SiO_2 –8 MgO –10 CaO –12 Na_2O (mol%, confirmed by inductively-coupled plasma mass spectrometry). After grinding in a porcelain mortar, the batch mixture was melted in a platinum crucible at 1500 °C for 2 h. Subsequently, the melt was poured into a graphite mould and annealed at 530 °C for 1 h before cooling to room temperature. From the obtained glass slab, individual samples were cut to dimensions of 10 mm × 7.5 mm × 0.5 mm and polished on both faces to optical grade using CeO_2 powder.

Compression method. Hot-compression was performed in accordance with established protocols^{29,30} at the ambient-pressure glass transition temperature ($T_g = 533$ °C) in two separate runs (1 GPa and 2 GPa), using a multizone cylindrical graphite furnace placed inside a gas pressure reactor with nitrogen as the compression medium. Details on the compression procedure and supplementary physical data of the employed glass are provided in Ref.³¹, which used the exact same glass as reference material (denoted SG0 in Ref.³¹). X-ray diffraction (Rigaku Miniflex 600) on the recovered glass samples did not reveal any evidence of crystallization following hot-compression treatment.

Analytical methods. *Raman scattering spectroscopy.* Raman spectroscopic measurements were performed using a Renishaw inVia confocal Raman microscope equipped with a low-frequency notch filter for collecting vibrational spectra in the frequency-range of 0–200 cm^{-1} . Samples were excited with an Argon ion (Ar^+) laser emitting at 514.5 nm. The light was focused into the sample and collected using a confocal microscope with a 50× objective. The scattered light was directed to a Rayleigh-line rejection filter to block the excitation laser light. All spectra were recorded in two polarization geometries, VV and VH, over a wavenumber region of 10–1380 cm^{-1} with 2 cm^{-1} resolution (using a diffraction grating with 2400 lines/mm). The polarization was controlled by means of a polarizer/half-wave plate set-up inserted in the laser beamline between the notch filter and the monochromator.

Nuclear magnetic resonance spectroscopy. ^{29}Si NMR MAS spectra were collected on a Q-OneTec 500 MHz spectrometer operating at 11.7 T (99.3 MHz for Si) equipped with a 7 mm rotor and spinning at 5 kHz. For this, samples were crushed manually using a mortar and pestle. Relaxation delays of 600 s were required for complete relaxation of a 90° pulse (8 μs), allowing for only 128 free-induction decays to be collected per sample. Chemical shifts were referenced to tetramethylsilane (TMS) and the spectrometer field was shimmed directly before data collection to obtain a sharp reference peak (38 Hz). Care was taken to collect a stator background spectrum with the same experimental conditions and subtract it from all samples. Due to the expected small differences between spectra, only a small exponential line-broadening (100 Hz) was applied during processing in TopSpin. After phasing in TopSpin, the spectra, including spinning sidebands, were deconvoluted in DmFit³² with all parameters being varied except for the spinning speed, which was locked at 5 kHz. The Monte Carlo error of the model was calculated for 600 replicates; the standard deviation of the replicates was used to determine the error for two standard deviation intervals (equal to the 95% confidence level). Additionally, the error from the peak width of the reference compound, TMS, was also added to the error of the peak positions and widths.

Ultrasonic echography. An echometer (Karl Deutsch GmbH & Co. KG) with a piezoelectric transducer operating in the frequency range of 8–12 MHz was employed to determine longitudinal and transversal sound wave propagation times, from which the transversal and longitudinal sound velocities (v_T and v_L) were deduced, and shear (G_{exp}), bulk (K_{exp}) and Young's (E_{exp}) moduli and Poisson's ratio ν were calculated.

Densities ρ were taken from Ref.³¹. The atomic packing density C_g , was estimated according to the MM model⁵ (Table 1).

SLMS glass samples	Density ³¹ (g/cm ³)	v_L (m/s)	v_T (m/s)	G_{exp} (GPa)	K_{exp} (GPa)	E_{exp} (GPa)	ν	C_g
pristine	2.563 ± 0.002	5703 ± 10	3408 ± 4	29.8 ± 0.1	43.7 ± 0.4	72.8 ± 0.7	0.222 ± 0.003	0.508
1 GPa	2.630 ± 0.002	5845 ± 10	3477 ± 4	31.8 ± 0.1	47.5 ± 0.5	78.0 ± 0.8	0.226 ± 0.003	0.521
2 GPa	2.683 ± 0.002	5944 ± 10	3534 ± 4	33.5 ± 0.1	50.1 ± 0.5	82.2 ± 0.8	0.227 ± 0.003	0.532

Table 1. Physical and macroscopic (experimental) mechanical properties of investigated glasses: density ρ , longitudinal and transversal sound wave velocity (v_L and v_T), shear modulus G_{exp} , bulk modulus K_{exp} , Young's modulus E_{exp} , Poisson's ratio ν and calculated atomic packing density C_g .

HET-CPA implementation. We recently reported on the implementation of HET-CPA for classifying the vibrational spectra of real-world glasses in terms of elastic disorder²⁸, considering that CPA is a highly reliable spectral theory of disorder^{33,34}. In the present study, we apply the same procedure to study the effect of densification while keeping the glass' bulk chemical composition unchanged. In short, the approach requires polarized VV and depolarized VH low-frequency Raman spectra, longitudinal and transversal sound wave velocity (v_L and v_T), and the Debye wavenumber $k_D = \sqrt[3]{6\pi^2\rho/\bar{m}}$ with the average atomic mass \bar{m} and the mass density ρ for input. From these data, the vibrational density of states (VDoS) and the probability density distribution of the local shear modulus $P(G)$ are obtained, from which the geometric mean G_0 and the disorder parameter σ^2 are extracted. In addition, we obtain the momentum cut-off $k_e = \sqrt[3]{2\pi^2/V_c}$, with the coarse-graining volume V_c used to define the local shear moduli G_i . In order to justify treating G_i as independent random variables, $\xi_c = \sqrt[3]{V_c}$ must be of the order of the correlation length ξ_G of the local fluctuations. We make the ansatz $k_e = A_\xi/\xi_G$ (with $A_\xi = 11.4$). Since the fitting procedure of the experimental data to the HET-CPA equations is ill-posed, regularization is required²⁸.

The non-affinity parameter n is obtained from the difference between the macroscopic (experimental) shear modulus and the geometric mean, $n = 1 - G_{\text{exp}}/G_0$ (where G_{exp} is always lower than G_0). The values of G_0 , n and ξ_G are used as quantifiers of elastic heterogeneity and disorder (with n being directly related to σ^2).

The obtained parameters were employed to reconstruct a two-dimensional glass with the shear modulus distribution $G(x, y)$ in silico. For this, we generated spatially correlated (2D isotropic) maps of random shear moduli which match the distribution function of $P(G)$. In order to avoid extreme spikes in those maps, we cut 10% of the area of the $P(G)$ from the right (where G approaches infinity). For spatial correlation, the random maps were convoluted with a Gaussian decay function with a standard deviation of $\xi_G/(2\sqrt{2})$. The convolution was done by multiplication in Fourier space, followed by inverse Fourier transformation. The corresponding spatial distribution of strain energy was calculated through finite element analysis of the two-dimensional HET equation in the frequency domain, with an additional harmonic stimulation on one of the four boundaries of the isotropic "2D glasses", and spatially invariant Poisson's ratio and mass density. We initially identified about 200 eigenmodes around the VDoS Boson peak position, and subsequently calculated the frequency response (total displacement field, total strain energy) at a frequency chosen near the resonance (the response spectra for the two examples shown in Fig. 4 are provided in Fig. S4). Thereby, *strain energy* denotes the total elastic energy density U_s (J/m³) at pixel resolution in 2D, derived from the stiffness tensor \mathbf{C} and the elastic strain tensor $\boldsymbol{\epsilon}_{\text{elastic}}$ under the assumptions of linear elasticity and zero initial stress. Since the simulation is in the frequency domain, values of U_s are time-averaged over one period.

Results and discussion

Structural characterization. Overview spectra of polarized VV and depolarized VH Raman scattering are shown in Fig. S1a,b, respectively, for the pristine and the hot-compressed SLMS glasses. For frequencies > 200 cm⁻¹, the Raman scattering bands of soda-lime silicate glasses are well documented in literature³⁵⁻³⁸, and also the effect of hot-compression to 2 GPa was reported previously³¹. In short, hot-compression at such comparably low pressure does not lead to significant changes in the intermediate-frequency region of the Raman spectra, in particular, in the depolarized case. Furthermore (other than in cold-compression experiment), the liquid fully relaxes into the compressed state while pressure is applied; after cooling and decompression at room temperature, the applied pressure corresponds to the *fictive pressure* p_f of the obtained glass. The only notable variation in the Raman scattering is in the main band $\Delta L_{1/2}$ (the half width at half maximum) of the VV spectrum, which exhibits a slight upshift, increases in intensity and becomes somewhat sharper with increasing compaction (Fig. S1c,d). These observations indicate a slight overall increase in phonon energy due to decreasing average atomic distance and a sharper distribution of the Si-O-Si angles³⁹⁻⁴¹.

To further observe the structural changes caused by hot-compression, we turned to ²⁹Si MAS NMR spectroscopy. In Fig. 1a, a clear trend is seen in the evolution of the ²⁹Si central peak as a function of applied pressure. This indicates that the pressure effect is preserved after crushing the sample for NMR analyses. On closer inspection, there is a consistent increase in chemical shift (indicating more shielded nuclei) with increasing compaction (Fig. 1b). Peak deconvolution (shown by way of example for the pristine glass sample in Fig. 1c, and for the compacted samples in Fig. S2) indicates dominance of mostly Q³ and Q⁴ structural units, with a minor amount of Q² and Q¹. This is to be expected based on the modifier-to-silica ratio of the SLMS glass. Although NMR studies of similar glasses (in particular, soda-lime silicate without MgO^{42,43}) used only two peaks (Q³ and Q⁴ units) to fit the ²⁹Si band for this ratio of glass former to glass modifier, we found that four peaks were needed to reproduce the central peak adequately. This is possibly due to our base glass composition having larger

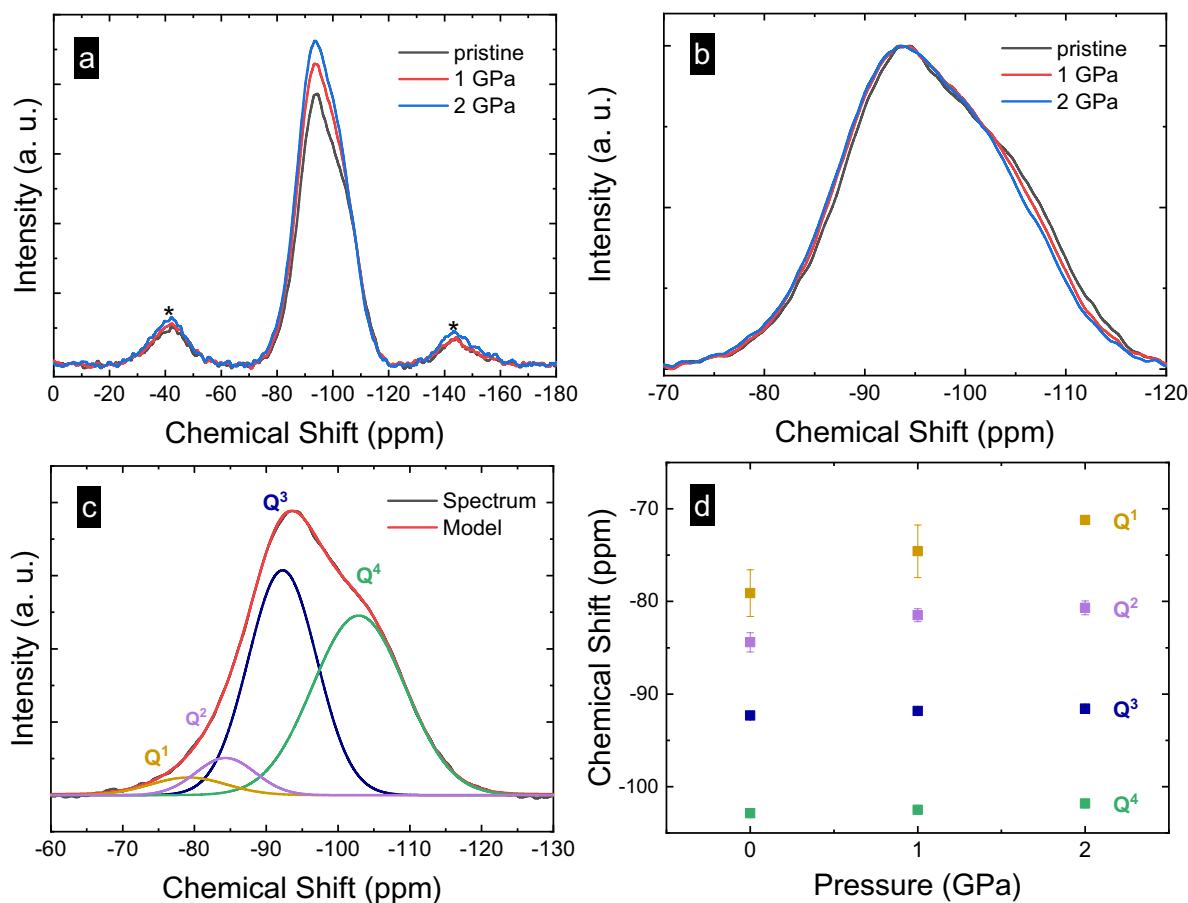


Figure 1. (a) ^{29}Si MAS NMR spectra of SLMS glasses taken from pristine (0.1 MPa) and hot-compressed samples (1 GPa and 2 GPa); (b) Close-up of intensity normalized ^{29}Si MAS NMR spectra; (c) Deconvolution of spectrum for the pristine glass; (d) Chemical shift parameters of SLMS glasses as a function of pressure during hot-compression.

amounts of MgO (possibly producing four-coordinated Mg^{2+} sites that may require charge compensation) and CaO (rather than Na_2O), since alkaline earth ions are known to increase the disproportionation reaction and lead to a larger spread of Q^n units⁴⁴. In fact, it was argued that alkaline earth silicates are consistently underfit, and that five peaks (Q^0 – Q^4) should be used. Nonetheless, fitting the spectra with more than four Q^n -unit peaks was not necessary in our case. The fitting of the spinning sidebands, in addition to the central peak, resulted in very reliable fits, as can be seen in the small error (see Table 2).

The chemical shift values (Fig. 1d and Table 2) are in-line with observations on other soda-lime silicates^{42,45}, although the present results are generally on the low side of the reported ppm range, likely due to the presence of magnesium. Indeed, this is especially true for our Q^4 chemical shift value (~ -103 ppm), whereas pure crystalline SiO_2 compounds have their Q^4 peaks located < -107 ppm (and have a mean Si–O–Si angle of $> 143.2^\circ$ ^{45,46}). When we use equations relating chemical shift to average $\angle\text{Si–O–Si}$ bond angle for Q^4 units only (from either Malfait et al.⁴⁶ or Oestrike et al.⁴⁷), we calculate an apparent average value of 135.3° for the Q^4 units in our pristine sample (Table 2). This is much lower than the mean $\angle\text{Si–O–Si}$ of 149° of compositionally similar soda-lime glasses reported by X-ray diffraction⁴⁸ or molecular dynamics simulation studies^{49,50}. There are many explanations for this difference. Modifying cations, even though not directly connected to Q^4 -units can have large influences on the NMR peak position^{51,52}, with MgO known to cause a more deshielded Si nucleus (higher ppm)⁵³. Although insufficient relaxation times have also been known to affect ^{29}Si chemical shifts⁴⁶, short delays result in higher ppm, not lower ppm as we observe here.

Next, we note that in a soda-lime silicate glasses, a Si–O–Si bond necessarily involves another SiO_4^{4-} tetrahedron, therefore, some Q^4 -units are necessarily connected to Q^2 - and Q^3 -units. Given that Q^2 units in diopside and α - CaSiO_3 have $\angle\text{Si–O–Si}$ of 135.93° and 135° ^{54,55}, respectively, and Q^3 units in crystalline $\text{Li}_2\text{Si}_2\text{O}_5$ and α - $\text{Na}_2\text{Si}_2\text{O}_5$ have $\angle\text{Si–O–Si}$ of 128° and 138.93° in the presence of a cation^{56–58}, respectively, an average Q^4 Si–O–Si angle of 135.3° appears to be physically reasonable for a modified silicate composition⁵⁷. This is further corroborated by our calculated Si–Si distance for the ambient pressure sample, 3.043 Å (assuming constant Shannon-Prewitt ionic radii⁵⁹, although the Si–O bond has been found to lengthen with pressure, it is a much smaller effect, only 0.02 Å reduction⁶⁰), which is in agreement with the both the X-ray diffraction data (3.14 Å)⁴⁸ and observations on silicate crystals with similar composition (3.0–3.1 Å)⁶¹.

²⁹ Si MAS NMR fit parameters		Samples		
		Pristine	1 GPa	2 GPa
Chemical shift (ppm)	Q ¹	-79 ± 3	-75 ± 3	-71.2 ± 0.5
	Q ²	-84 ± 1	-81.5 ± 0.7	-80.7 ± 0.7
	Q ³	-92.3 ± 0.2	-91.8 ± 0.09	-91.6 ± 0.1
	Q ⁴	-102.9 ± 0.2	-102.5 ± 0.3	-101.8 ± 0.3
Peak width (ppm)	Q ¹	12 ± 2	7 ± 3	3 ± 1
	Q ²	10 ± 1	9 ± 2	10.6 ± 0.9
	Q ³	11.2 ± 0.4	12.5 ± 0.4	12.5 ± 0.3
	Q ⁴	15.2 ± 0.2	14.6 ± 0.2	14.8 ± 0.2
Relative area (%)	Q ¹	4 ± 2	1 ± 1	0.11 ± 0.06
	Q ²	7 ± 4	4 ± 2	5 ± 1
	Q ³	43 ± 4	51 ± 3	48 ± 3
	Q ⁴	47 ± 1	44 ± 2	45 ± 2
($\langle \text{Si-O-Si} \rangle$ only)		135.3	134.7	133.5
Si-Si (Å)		3.034	3.027	3.014
% -volume reduction		-	-0.69	-1.95
[NBO]/[O]		0.29 ± 0.03	0.27 ± 0.02	0.26 ± 0.02
[NBO]/[Si]		0.67 ± 0.07	0.61 ± 0.04	0.59 ± 0.04

Table 2. Deconvolution parameters for ²⁹Si MAS NMR spectra of SLMS glasses obtained for pristine (ambient) and hot-compressed (1 GPa and 2 GPa) samples. Chemical shifts of Qⁿ units, peak width, relative abundance (%) of Qⁿ species, calculated average $\langle \text{Si-O-Si} \rangle$ bond angle, Si-Si distance, volume reduction and average number of non-bridging oxygen per silicon atom [NBO]/[Si] and oxygen atom [NBO]/[O].

Rather than further discussing the absolute value of the bond angle, in the following, we focus on the relative effect of densification, *i.e.*, the narrowing of the Si-O-Si bond-angle of Q⁴ units only (not Q² and Q³), simply because it is the most well-studied and, therefore, potentially reliable trend related to the ²⁹Si chemical shift. Indeed, Mackenzie and Smith⁶² caution against combining chemical shift and $\langle \text{Si-O-Si} \rangle$ data into a single relationship, as the chemical shift is greatly affected by next-nearest neighbors; therefore, it can strictly be applied only to alike materials. It is much more challenging to understand the structural changes in chemical shift for the Q² and Q³ units, partly because there are no model systems with our exact glass composition, but also because of the action of the modifying cation to pressure. For diopside crystals (MgCaSi₂O₆, all Q²) under pressure, it was found that the volume of the modifier cation coordination sphere compresses much more than that of the SiO₄⁴⁻ tetrahedron, 2.5% vs. <math>< 1\%</math>, respectively, for pressures between ambient and 2.36 GPa; in fact Levien and Prewitt⁶³ found that the compression of diopside is controlled by the ‘directions’ and compressibilities of the bonds in the cation polyhedra and not by the chains of the silicate tetrahedra—thus, the exact way in which densification manifests itself on short-range order in the present glasses remains unclear, especially regarding Q² and Q³-units and their neighbouring cations.

Using the reduction of the Si-Si distance, which is caused by the narrowing of the Si-O-Si angle in Q⁴ units, we find a corresponding volume reduction of 0.69% and 1.95% for hot-compression at 1 and 2 GPa, respectively. This compares to the respective macroscopic densification of 2.61% and 4.66% observed in mass density³¹. The difference arguably reflects the preferential compaction of ‘soft’ cation sites⁶⁴, which are not fully reflected in the Si-O-Si angle when only Q⁴ units are considered in the analysis of densification (as the relation between the chemical shift of Q² or Q³ and the involved Si-O-Si bond angle is unknown⁶²). Again, we are unsure about the exact structural response of the Q²- and Q³-units upon densification, except that their chemical shifts generally increase under pressure, too (in ppm), indicating a narrowing of the average $\langle \text{Si-O-Si} \rangle$. However, the magnitude of the narrowing is unknown.

In a more in-depth ¹⁷O NMR study of pure SiO₂ crystals and glasses⁶⁰, pressures of 8 and 13.5 GPa, respectively, were found to decrease the Si-O-Si angle significantly (with an increase in mean Si-O bond length). This study also noted that there may be a hard limit to the sharpest energetically favourable $\langle \text{Si-O-Si} \rangle$, 130°, and rather than all angles necessarily decreasing equally, sharper $\langle \text{Si-O-Si} \rangle$ simply became more prevalent (which decreased the average $\langle \text{Si-O-Si} \rangle$). The width of the bond-angle and bond-distance distributions did not change significantly, however, the shape of the $\langle \text{Si-O-Si} \rangle$ distribution changed, becoming more Lorentzian in shape (where even extreme $\langle \text{Si-O-Si} \rangle$ values have significant population). This is an example of a structural preference affecting the shape of the probability distribution, which could lead to ill-fitted parameters if not taken into consideration.

The fraction of different Qⁿ species corresponds to what has been reported elsewhere⁴⁹ in the case of a similar manganese-containing soda-lime silicate glass (72.2 SiO₂-5.5 MgO-8.9 CaO-12.3 Na₂O-1.1 Al₂O₃ (mol%)). In particular, the Q⁴ species population was found to be higher than that of Q³, Q² or Q¹, which supports the relevance of our deconvolution. The [NBO]/[O]_{NMR} ratio calculated from NMR, 0.238, is somewhat lower than that expected from composition, 0.34, and that from a soda-lime silicate glass of similar composition without MgO, 0.29⁴², we believe that the presence of Mg²⁺ could be the reason for this observation⁶⁵. The small decrease in [NBO]/[O] in Table 2 is concomitant with an increase in ‘free oxide’ (FO) according to 2 NBO → 1 BO + FO,

which may confirm that under compression, there is preferential compaction of soft ion sites. More importantly, we do not expect a large change in $[NBO]/[O]$ at the relatively low pressures we applied here (Table 2).

Elastic heterogeneity and compaction-induced homogenization. An example of fitting low-frequency Raman data using HET-CPA is provided in Fig. 2a for the pristine glass sample. The spectrum is displayed in reduced scale, $I_{red}(\omega, T) = I_n(\omega, T)/[m(\omega, T) + 1]^{27}$. The function $n(\omega, T)$ is the Bose–Einstein distribution function for the phonon occupation at frequency ω and temperature T . The HET-CPA data fit reproduces the spectral shape of the reduced low-frequency Raman spectrum ($< 200 \text{ cm}^{-1}$), with a standard error regression error of $S=0.071$ (in the range $30\text{--}200 \text{ cm}^{-1}$). All output parameters are listed in Table 3. We note that HET underestimates the experimental Raman scattering intensity for $\omega \rightarrow 0$, as $I(\omega) \propto \omega^{266}$. This is related to quasi-elastic scattering (QES)⁶⁷, which is not considered in HET.

Figure 2b depicts the reduced VDOS from HET-CPA for pristine and hot-compressed glasses. From these spectra, the Boson peak frequency ω_{BP} (VDoS) is extracted as the frequency at which $g(\omega)/\omega^2$ reaches its maximum. It shifts toward higher frequencies and decreases in intensity $I_{BP} = \max[g(\omega)/\omega^2]$ with hot-compression at increasing pressure. Similar observations have already been made in semi-empirical studies of hot- or cold-compressed glasses (mostly using empirical coupling factors for obtaining VDoS from Raman scattering data)^{68–70}. The up-shift of ω_{BP} is usually related to a qualitative decrease in the length scale of heterogeneity^{71,72}, and the decrease in intensity indicates a decrease in the number of soft modes. Evaluation by HET now provides a quantitative and purely physical basis for this conjecture^{28,73,74}.

Comparing the vibrational properties of different solids requires prior scaling (normalization) with the continuous medium properties expressed in terms of the Debye frequency ω_D and the Debye level A_D ($g_D(\omega) = A_D \omega^2$)⁷⁵. We now verify whether the shift of ω_{BP} (VDoS) and the decrease of its amplitude I_{BP} (or $\max[g(\omega)/\omega^2]$), observed in Fig. 2b represent a deviation from continuous medium transformation, that is, non-affinity. For this, we compare first the density dependence of ω_{BP} and that of ω_D (with $\omega_D \approx (9\pi^2 \rho)^{1/3} \sqrt{G_{exp}/\rho}$)⁷⁶ as reported in Fig. 2c. Furthermore, the variation of the Boson peak amplitude I_{BP} ($\max[g(\omega)/\omega^2]$) is compared to the variation of the Debye level A_D (with $A_D = 3\omega_D^{-3} \approx [3\pi^2 \rho (G_{exp}/\rho)^{-3/2}]^{-1}$)⁷⁶ as shown in Fig. 2d. Both datasets in Fig. 2c,d are normalized to a reference value (we use the mass density at room temperature). In Fig. 2c, we observe that the frequency shifts induced by hot-compression are about one order of magnitude higher than those of the Debye frequency. A similar behavior is observed in Fig. 2d, where changes of the Boson peak intensity systematically exceed the changes in the Debye level. These findings are consistent previous studies of hot and cold-compressed glasses and polymers^{76–78} which clearly demonstrate that the glass does not behave as an isotropic, homogeneous elastic continuum, at least upon compression. As the continuum medium properties (ω_D and A_D) are mostly determined from the macroscopic shear modulus G_{exp} , we deduce that non-affine compression (preferential compression of soft modes) affects not only the macroscopic shear modulus G_{exp} (+12.5%), but also its spatial fluctuation⁷⁶. During the last decade, various studies have been carried out with the aim to explain the non-Debye scaling (the failure of scaling observed in Fig. 2c,d) during densification^{68,78,79}, variations in cooling rates^{80,81} or adaptations of chemical composition⁸². Examining a broad range of glass compositions, two phenomenological correlations were recently discovered which link vibrational disorder and boson peak parameters to fluctuating elasticity²⁸. First, a one-to-one correlation was found between the characteristic frequency $\omega_0 = k_e \sqrt{G_0/\rho}$ and the VDoS Boson peak position, $\omega_{BP} = 0.333\omega_0$. Secondly, a power-law relationship was revealed for the Boson peak intensity, $\omega_0^3 \max[g(\omega)/\omega^2] = 2.19((k_e/k_d) \times (1/1 - n))^{2,42}$. Both of these relations exhibited applicability to the broadest range of glass chemistries. Interestingly, this also appears to hold when the chemical composition is kept unchanged, but the fictive pressure (and thus, glass density) is varied: in Fig. 2e,f, we show that the present compacted SLMS glasses also fall perfectly into the reported trend (it remains to be explored how this will hold for other glass compositions, or when the observed range of pressures is extended).

The population density distributions of the shear modulus of pristine and hot-compressed SLMS glasses are presented in Fig. 3a. Our choice of a log-normal distribution was initially motivated by the assumption that the fluctuation in shear modulus (in the glassy state) is related to liquid dynamics (in the melt from which the glass was originally derived). The validity of this approach is confirmed by Köhler et al.⁸³, who emphasized the suitability of log-normal distributions in covering sufficiently high degrees disorder to represent real-world glasses (over uniform or truncated Gaussian functions).

As shown in Fig. 3b, the typical shear modulus G_0 (the geometric mean of the log-normal distribution) increases linearly with densification. This is intuitively expected, because also the macroscopic shear modulus G_{exp} increases (Table 1). However, on closer inspection, we find that G_0 seems to be less affected by densification as compared to the macroscopic shear modulus, with an increase of 10.6% versus ~12.4% observed after hot-compression at 2 GPa. This is a direct manifestation of the deviation from the continuum medium transformation (CMT) model; it indicates non-affine compaction, whereby we may assume that ‘soft’ regions compact preferentially over more rigid regions, in accordance with our previous discussion of the variations in Si–O–Si angle observed by NMR.

Several explanations have been proposed for the variation of the macroscopic shear modulus G_{exp} with densification in different types of glasses, typically referring to the change of packing density or to variations in network topology (such as changes on the Si–O–Si angle and the distribution of ring sizes, the formation of highly-coordinated defect states or increasing coordination numbers on network-forming species). In our case, we obtain an increase in C_g by 4.72% for hot-compression at 2 GPa, see Table 1. This represents relatively mild compression, for which we do not expect significant variations on the Si coordination number⁸⁴ (in agreement with our NMR and Raman analyses).

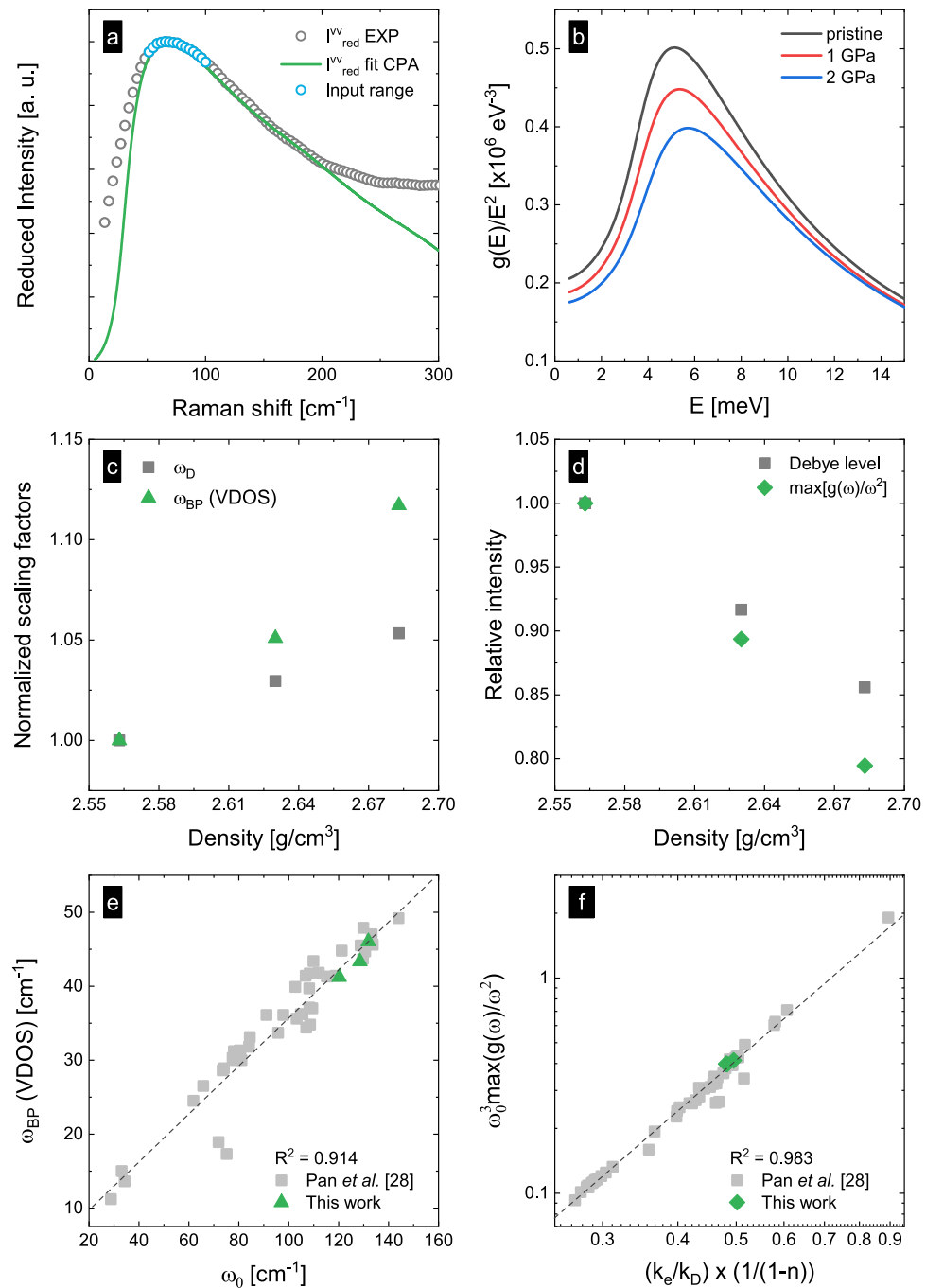


Figure 2. (a) Low-frequency Raman spectrum (reduced intensity $I_{\text{red}}^{\text{v}}$) of the pristine SLMS glass (grey scattered points) and HET-CPA fit (green solid line). The blue circles mark the input range of the fit (50–100 cm^{-1}). (b) Reduced vibrational density of states $g(E)/E^2$ obtained from HET-CPA for the pristine and the hot-compressed glasses. (c) Variation of the scaling factors relative to the Boson peak frequency ω_{BP} (VDOS) and to the Debye frequency ω_{D} as functions of the glass' mass density. (d) Variation of the relative intensity the Boson peak intensity I_{BP} (VDOS) and the Debye level as functions of the mass density. (e) Boson peak frequency ω_{BP} (VDOS) as a function of ω_0 . (f) Double-logarithmic plot of the maximum of $\omega_0^3 \max[g(\omega)/\omega^2]$ vs. $(k_e/k_d) \times (1/(1-n))$. The grey dashed lines in panels (e,f) are linear data fits (with slope of 0.33 in (e) and 2.42 in (f)).

Besides G_0 , the $P(G)$ is characterized by a second parameter, the disorder parameter σ^2 . As a result of hot-compression at 2 GPa, we observe a decrease in σ^2 by $\sim 7\%$ (noteworthy, σ^2 being a quadratic function in exponential space, Fig. 3d). This manifests in a significantly sharper $P(G)$, whereby the sharpening occurs through

SLMS glass samples	ω_{BP} (cm ⁻¹)	G_0 (GPa)	k_e (Å ⁻¹)	ξ_c (nm)	ξ_G (nm)	σ^2	n
Pristine	41.23 ± 0.79	39.57 ± 0.33	0.594 ± 0.013	0.455 ± 0.010	1.917 ± 0.042	0.985 ± 0.032	0.247 ± 0.006
1 GPa	43.33 ± 0.34	41.89 ± 0.22	0.607 ± 0.005	0.445 ± 0.04	1.875 ± 0.016	0.957 ± 0.020	0.241 ± 0.004
2 GPa	46.06 ± 0.85	43.77 ± 0.41	0.632 ± 0.019	0.428 ± 0.013	1.803 ± 0.050	0.924 ± 0.036	0.234 ± 0.007

Table 3. Model output parameters: Boson peak position ω_{BP} (VDoS), geometric mean shear modulus G_0 , momentum cut-off k_e , coarse-graining length ξ_c , correlation length ξ_G , disorder parameter σ^2 and non-affinity n .

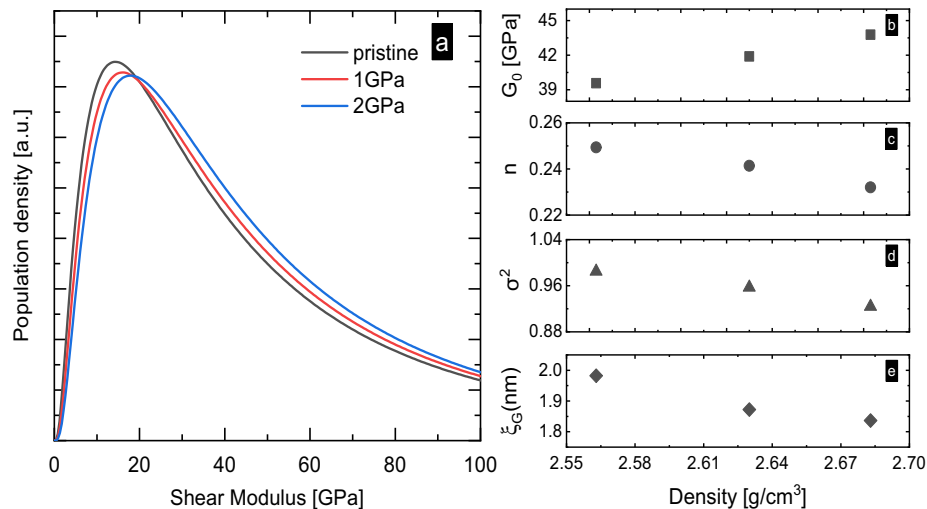


Figure 3. (a) Population density distributions of local shear modulus $P(G)$ of SLMS glasses in their pristine state and after hot-compression (1 GPa and 2 GPa). (b) Typical shear modulus (geometric mean) G_0 , (c) non-affinity parameter n , (d) disorder parameter σ^2 and (e) characteristic length ξ_G as functions of mass density.

the reduction of ‘soft modes’: the high-modulus boundary of $P(G)$ is almost unaffected by hot-compression, whereas the shift occurs on the lower edge. This relative decrease in the number of ‘soft modes’ causes a decrease in the difference between the macroscopic modulus G_{exp} and the geometric mean G_0 ²⁸ and, thus, a decrease in the non-affinity parameter n (in the present case, by about 5.5% following hot-compression at 2 GPa, Fig. 3c). This result is in agreement with that of Pan et al.²⁸; as shown in Fig. S3, the non-affine reduction of the macroscopic shear modulus G_{exp} occurs in a wide range of glasses.

With the variations in $P(G)$, the correlation length ξ_G decreases by $\sim 6\%$ after hot-compression at 2 GPa (Fig. 3e). This compares to a simultaneous change in packing density by $\sim +4.7\%$ (Table 1) and again reflects the deviation from the CMT approximation, where the effect of compression on ω_{BP} is two to three times as high as the one on ω_D (inset of Fig. 2c). It is interesting to note that this roughly matches the amount by which the variation of ξ_G exceeds the expectation derived from the (macroscopic) packing density alone. The ‘excess’ of ξ_G variation appears to be related to the decrease in non-affinity; both parameters affect the position of the boson peak²⁸ and, therefore, the deviation from CMT.

Two-dimensional in silico reconstructions of the HET-CPA parameters of the pristine and compressed SLMS glasses are shown in Fig. 4. They act as two-dimensional representations of $P(G)$, assuming random spatial fluctuation with an autocorrelation length of ξ_G . Therefore, while all physical information is strictly contained within the parametric descriptors, the reconstructions provide visual access for further interpretation of the effect of hot-compression. As the primary features, both the decreasing length scale and the decreasing non-affinity are reflected in these maps, with the microstructure becoming more fine-grained as a result of hot-compression. The strain energy maps reflect the response of a material with the constructed $G(x,y)$ (that is, for disorder statics reflecting those of the present SLMS glasses) to acoustic stimulation. Clearly, the strain energy becomes more homogeneously distributed as a result of compaction, with softer regions (low G) decreasing in size and less-intense local spikes in stored energy, thus, more homogeneous energy distribution (whereby sound transport occurs preferentially across the percolating hard regions: the strain energy maps provide a clear rationale for the increase in macroscopic elastic moduli as a result of compaction, which exceeds the CMT prediction).

Possible relations between structural heterogeneity, glass densification and variations on short and intermediate range order have been discussed on various occasions^{85–87}, often making use of the ‘non-continuous structure model’^{72,88}. This model conjectures a relation between ω_{BP} and the characteristic size and shape of rigid, dispersed objects in a model morphology of ‘cohesive’ and ‘soft’ nanodomains. The size of the characteristic length scale proposed by the non-continuous structure model is on the same order of magnitude as the one found through

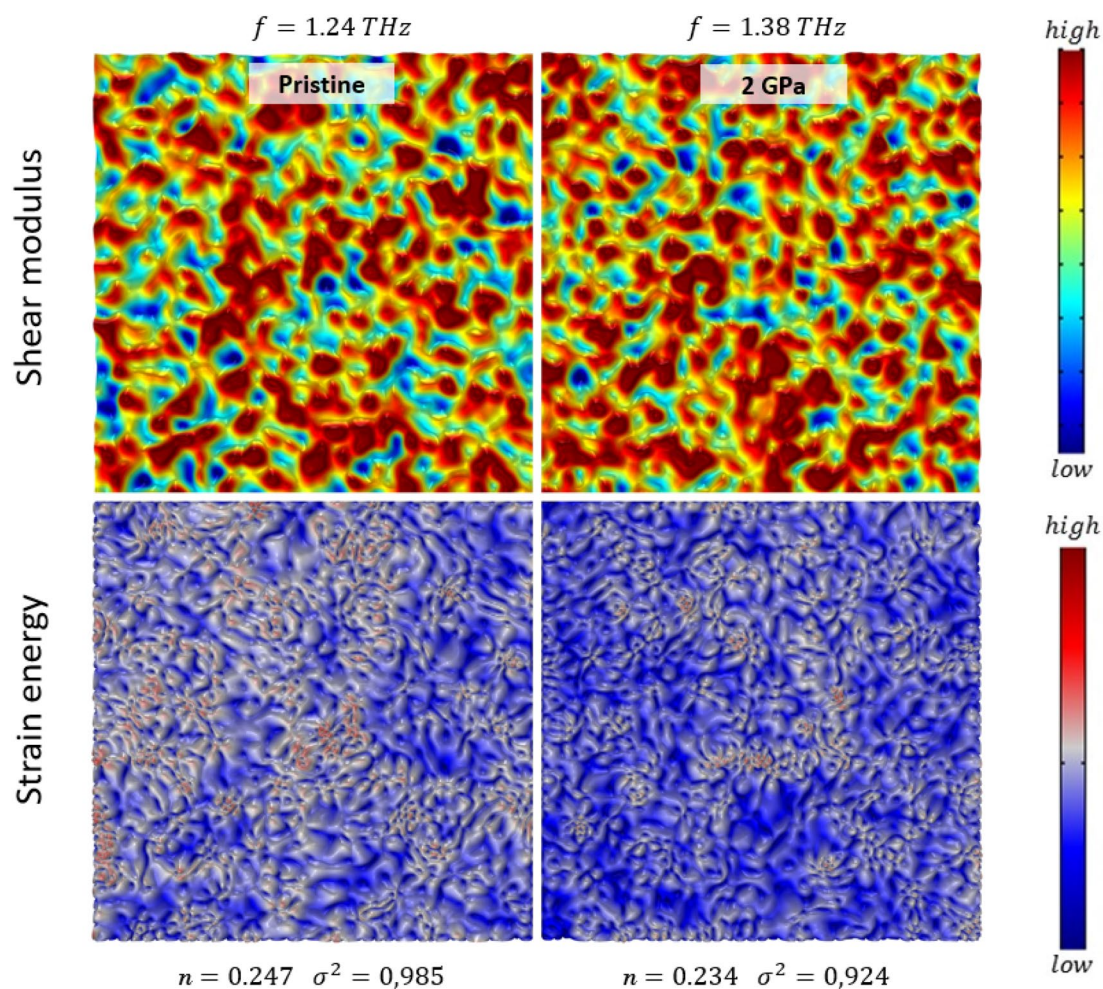


Figure 4. (top) Real-space two-dimensional reconstruction of the local elastic heterogeneity $G(x,y)$ as obtained for pristine and hot-compressed (2 GPa) SLMS glass by HET-CPA. The image size is $50 \text{ nm} \times 50 \text{ nm}$. The top-label indicates the resonance frequency used for excitation in the strain energy maps (bottom). The corresponding non-affinity parameter n and the disorder parameter σ^2 are indicated below the strain energy panels.

HET in silico¹⁹ or HET supplied with experimental data for the broadest range of glass chemistries²⁸, however, the descriptors obtained through HET-CPA have clear physical meanings. For example, instead of an empirical shape factor for dispersed nano-objects, we obtain direct access to non-affinity and a more realistic morphology such as depicted in Fig. 4. An interesting explanation for elastic homogenization following structural compaction beyond CMT was brought forth by Leonforte⁸⁹. Using mode-projection analysis, it was shown for some glass formers (SiO_2 ^{90,91}, P_2O_5 ⁹²) that the 'boson peak' is related to rotational (F_1) modes of network-forming tetrahedra. The tetrahedra may rotate in directions opposite or similar to their neighbours. In such cases, elastic homogenization following densification can be related to the competition between connected tetrahedral units with similar and with opposing rotation. Increasing the pressure constrains the number of opposing inter-tetrahedral rotations, thereby reducing inhomogeneous particle rearrangements⁸⁹.

Conclusions

In summary, we studied the effect of structural compaction on the statistics of elastic disorder in a soda lime magnesia silicate glass. HET-CPA was used with THz Raman spectroscopic data to extract variations in the log-normal distribution of the local shear modulus for densification by up to 5%. These variations were found to occur primarily on the soft end of the distribution, as also reflected in a decrease in the non-affine part of the shear modulus; compaction occurred preferentially in soft modes, which lead to overall homogenization of the spatial strain energy distribution. The pressure-induced increase in macroscopic elastic moduli is attributed to this homogenization effect (which exceeds the continuous medium approximation). Within the considered pressure range, hot-compression of SLMS glasses reveals the same relationship between the boson peak position and the (local) characteristic frequency as was previously reported for the broadest variability of glass chemical compositions. It remains to be explored how experiments at higher pressure and/or the use of glasses with variable pressure dependence of (short-range) structural motifs would further affect this picture.

Data availability

The data that support the findings of this study are shown in the manuscript or supporting information, or available from the corresponding author on reasonable request.

Received: 6 August 2021; Accepted: 14 December 2021

Published online: 27 December 2021

References

- Wondraczek, L. *et al.* Towards ultrastrong glasses. *Adv. Mater.* **23**, 4578–4586 (2011).
- Wondraczek, L. *et al.* Advancing the mechanical performance of glasses: perspectives and challenges. *Adv. Mater.* **34**. <https://doi.org/10.1002/adma.202109029> (2022).
- Rouxel, T. Elastic properties and short-to medium-range order in glasses. *J. Am. Ceram. Soc.* **90**, 3019–3039 (2007).
- Phillips, C. J. Calculation of Young's modulus of elasticity from composition of simple and complex silicate glasses. *Glass Technol.* **5**, 216–223 (1964).
- Makishima, A. & Mackenzie, J. D. Direct calculation of Young's modulus of glass. *J. Non-Cryst. Solids.* **12**, 35–45 (1973).
- Rocherulle, J., Ecolivet, C., Poulain, M., Verdier, P. & Laurent, Y. Elastic moduli of oxynitride glasses: Extension of Makishima and Mackenzie's theory. *J. Non-Cryst. Solids.* **108**, 187–193 (1989).
- Wilkinson, C. J., Zheng, Q., Huang, L. & Mauro, J. C. Topological constraint model for the elasticity of glass-forming systems. *Non-Cryst. Solids: X* **2**, 100019 (2019).
- Yang, K. *et al.* Predicting the Young's modulus of silicate glasses using high-throughput molecular dynamics simulations and machine learning. *Sci. Rep.* **9**, 8739 (2019).
- Rodrigues, B. P., To, T., Smedskjaer, M. M. & Wondraczek, L. Mechanical properties of oxide glasses. *Rev. Mineral. Geochem.* **87**. <https://doi.org/10.2138/rmg.2021.87.07> (2022).
- Plucinski, M. & Zwanziger, J. W. Topological constraints and the Makishima–Mackenzie model. *J. Non-Cryst. Solids.* **429**, 20–23 (2015).
- Pönitzsch, A., Nofz, M., Wondraczek, L. & Deubener, J. Bulk elastic properties, hardness and fatigue of calcium aluminosilicate glasses in the intermediate-silica range. *J. Non-Cryst. Solids.* **434**, 1–12 (2016).
- Limbach, R., Rodrigues, B. P., Möncke, D. & Wondraczek, L. Elasticity, deformation and fracture of mixed fluoride–phosphate glasses. *J. Non-Cryst. Solids.* **430**, 99–107 (2015).
- Sawamura, S. & Wondraczek, L. Scratch hardness of glass. *Phys. Rev. Mater.* **2**, 092601(R) (2018).
- Yoshimoto, K., Jain, T. S., Workum, K. V., Nealey, P. F. & de Pablo, J. J. Mechanical heterogeneities in model polymer glasses at small length scales. *Phys. Rev. Lett.* **93**, 175501 (2004).
- Tsamados, M., Tanguy, A., Goldenberg, C. & Barrat, J.-L. Local elasticity map and plasticity in a model Lennard-Jones glass. *Phys. Rev. E* **80**, 026112 (2009).
- Zhang, L. *et al.* Echinochloa crus-galli genome analysis provides insight into its adaptation and invasiveness as a weed. *Nat. Commun.* **8**, 67 (2017).
- Wang, Y., Hong, L., Wang, Y., Schirmacher, W. & Zhang, J. Disentangling boson peaks and van hove singularities in a model glass. *Phys. Rev. B* **98**, 174207 (2018).
- Leonforte, F., Boissière, R., Tanguy, A., Wittmer, J. P. & Barrat, J.-L. Continuum limit of amorphous elastic bodies. Iii. three-dimensional systems. *Phys. Rev. B* **72**, 224206 (2005).
- Leonforte, F., Tanguy, A., Wittmer, J. P. & Barrat, J.-L. Inhomogeneous elastic response of silica glass. *Phys. Rev. Lett.* **97**(5), 055501 (2006).
- DiDonna, B. A. & Lubensky, T. C. Nonaffine correlations in random elastic media. *Phys. Rev. E* **72**, 066619 (2005).
- Maloney, C. E. Correlations in the elastic response of dense random packings. *Phys. Rev. Lett.* **97**, 035503 (2006).
- Mizuno, H., Mossa, S. & Louis Barrat, J. Relation of vibrational excitations and thermal conductivity to elastic heterogeneities in disordered solids. *Phys. Rev. B* **94**, 144303 (2016).
- Born, M. & Huang, K. *Dynamical theory of crystal lattices*. Oxford University Press (1955).
- Mizuno, H., Mossa, S. & Louis Barrat, J. Measuring spatial distribution of the local elastic modulus in glasses. *Phys. Rev. E* **87**, 042306 (2013).
- Wagner, H. *et al.* Local elastic properties of a metallic glass. *Nature Mater.* **10**, 439–442 (2011).
- Schirmacher, W. Thermal conductivity of glassy materials and the boson peak. *Europhys. Lett.* **73**, 892–898 (2006).
- Schmid, B. & Schirmacher, W. Raman scattering and the low-frequency vibrational spectrum of glasses. *Phys. Rev. Lett.* **100**, 137402 (2008).
- Pan, Z. *et al.* Disorder classification of the vibrational spectra of modern glasses. *Phys. Rev. B* **104**, 134106 (2021).
- Kapoor, S., Wondraczek, L. & Smedskjaer, M. M. Pressure-induced densification of oxide glasses at the glass transition. *Front. Mater.* **4**, 1–20 (2017).
- Wondraczek, L. & Behrens, H. Molar volume, excess enthalpy, and Prigogine–Defay ratio of some silicate glasses with different (P, T) histories. *J. Chem. Phys.* **127**, 154503 (2007).
- Cherbib, M. A., Kapoor, S., Bockowski, M., Smedskjaer, M. M. & Wondraczek, L. Luminescence behaviour of Eu³⁺ in hot-compressed silicate glasses. *J. Non-Cryst. Solids: X* **4**, 100041 (2019).
- Massiot, D. *et al.* Modelling one- and two-dimensional solid-state NMR spectra. *Magn. Reson. Chem.* **40**(1), 70–76 (2002).
- Elliott, R. J., Krumhansl, J. A. & Leath, P. L. The theory and properties of randomly disordered crystals and related physical systems. *Rev. Mod. Phys.* **46**, 465 (1974).
- Ebert, H., Ködderitzsch, D. & Minár, J. Calculating condensed matter properties using the KKR–Green's function method—recent developments and applications. *Rep. Prog. Phys.* **74**, 096501 (2011).
- Brawer, S. A. & White, W. B. Raman spectroscopic investigation of the structure of silicate glasses (II) Soda-alkaline earth-alumina ternary and quaternary glasses. *J. Non-Cryst. Solids.* **23**, 261–278 (1977).
- McMillan, P. Structural studies of silicate glasses and melts—applications and limitations of Raman spectroscopy. *Am. Mineral.* **69**, 622–644 (1984).
- Deschamps, T., Martinet, C., Bruneel, J. L. & Champagnon, B. Soda-lime silicate glass under hydrostatic pressure and indentation: A micro-Raman study. *J. Phys. Condens. Matter.* **23**(3), 035402 (2011).
- Wang, M., Cheng, J., Li, M. & He, F. Raman spectra of soda–lime–silicate glass doped with rare earth. *Phys. B Condens. Matter.* **406**, 3865–3869 (2011).
- Martin, C. *et al.* Permanently densified SiO₂ glasses: A structural approach. *Phys. Condens. Matter.* **27**, 325401 (2015).
- Cornet, A., Martinez, V., de Ligny, D., Champagnon, B. & Martinet, C. Relaxation processes of densified silica glass. *J. Chem. Phys.* **146**, 094504 (2017).
- Guerette, M. *et al.* Structure and properties of silica glass densified in cold compression and hot compression. *Sci. Rep.* **5**, 15343 (2015).

42. Jones, A. R., Winter, R., Greaves, G. N., Smith, I. H. & Non-Cryst, J. MAS NMR study of soda-lime-silicate glasses with variable degree of polymerisation. *J. Non-Cryst. Solids* **293–295**, 87–92 (2001).
43. Santos, C. N., Meneses, D. d. S., Montouillout, V. & Echegut, P. Infrared emissivity spectroscopy of a soda-lime silicate glass. arXiv:1201.5676 (2012).
44. Zhang, P., Grandinetti, P. J. & Stebbins, J. F. Anionic species determination in CaSiO₃ glass using two-dimensional ²⁹Si NMR. *J. Phys. Chem. B* **101**(20), 4004–4008 (1997).
45. Murdoch, J. B., Stebbins, J. F. & Carmichael, I. S. E. High-resolution ²⁹Si NMR study of silicate and aluminosilicate glasses: The effect of network-modifying cations. *Am. Mineral.* **70**, 332–343 (1985).
46. Malfait, W. J., Halter, W. E. & Verel, R. ²⁹Si NMR spectroscopy of silica glass: T1 relaxation and constraints on the Si–O–Si bond angle distribution. *Chem. Geol.* **256**, 269–277 (2008).
47. Oestrike, R. *et al.* ²⁷Al MAS NMR and aluminum X-ray absorption near edge structure study of imogolite and allophanes. *Geochim. Cosmochim. Acta.* **51**, 2199–2209 (1987).
48. Iwadate, Y., Hattori, T., Igarashi, K. & Mochinaga, J. Short-range structure of a multicomponent glass by an X-ray diffraction method. *J. Mater. Sci. Lett.* **7**, 891–892 (1988).
49. Taniguchi, T. & Ito, S. Molecular dynamics simulation of the structure of soda-lime-silica glass. *Rep. Res. Lab. Asahi Glass* **53**, 1 (2003).
50. Pedone, A., Malavasi, G., Menziani, M. C., Sesgre, U. & Cormack, A. N. Role of magnesium in soda-lime glasses: Insight into structural, transport, and mechanical properties through computer simulations. *J. Phys. Chem. C* **112**, 11034–11041 (2008).
51. Maekawa, H., Maekawa, T., Kawamura, K. & Yokokawa, T. The structural groups of alkali silicate glasses determined from ²⁹Si MAS-NMR. *J. Non-Cryst. Solids.* **127**, 53–64 (1991).
52. Brandriss, M. E. & Stebbins, J. F. Effects of temperature on the structures of silicate liquids: ²⁹Si NMR results. *Geochim. Cosmochim. Acta.* **52**, 2659–2669 (1988).
53. Oliveira, J. M., Correia, R. N., Fernandes, M. H. & Rocha, J. Influence of the CaO/MgO ratio on the structure of phase-separated glasses: A solid state ²⁹Si and ³¹P MAS NMR study. *J. Non-Cryst. Solids.* **265**, 221–229 (2000).
54. Cameron, M., Sueno, S., Prewitt, C. T. & Papike, J. J. High-temperature crystal chemistry of acmite, diopside, hedenbergite, jadeite, spodumene and ureyite. *Am. Mineral.* **58**(7–8), 594–618 (1973).
55. Yamanaka, T. & Mori, H. The structure and polytypes of α-CaSiO₃ (pseudowollastonite). *Acta Crystallogr. Sect. B* **37**, 1010–1017 (1981).
56. Liebau, F. Untersuchungen an schichtsilikaten des formeltyps Am (Si₂O₅) n. I. Die kristallstruktur der zimmertemperaturform des Li₂Si₂O₅. *Acta Crystallogr.* **14**, 389–395 (1961).
57. de Jong, B. H. W. S. *et al.* *Acta Cryst. B* **54**, 568–577 (1998).
58. Pant, A. K. & Cruickshank, D. W. J. Comprehensive derivation of bond-valence parameters for ion pairs involving oxygen. *Acta Crystallogr. Sect. B* **24**(1), 13–19 (1986).
59. Shannon, R. D. Revised effective ionic radii and systematic studies of interatomic distances in halides and chalcogenides. *Acta Crystallogr. A* **32**, 751–767 (1976).
60. Trease, N. M., Clark, T. M., Grandinetti, P. J., Stebbins, J. F. & Sen, S. Bond length-bond angle correlation in densified silica—Results from ¹⁷O NMR spectroscopy. *J. Chem. Phys.* **146**, 184505 (2017).
61. Thompson, R. M. & Downs, R. T. The crystal structure of diopside at pressure to 10 GPa. *Am. Mineral.* **93**(1), 177–186 (2008).
62. MacKenzie, K. J. D. & Smith, M. E. Multinuclear solid-state NMR of inorganic materials. *Pergamon Mater. Ser.* **6**, 201–268 (2002).
63. Levien, L. & Prewitt, C. T. High-pressure structural study of diopside. *Am. Mineral.* **66**, 315–323 (1981).
64. Wu, J. *et al.* Structural response of a highly viscous aluminoborosilicate melt to isotropic and anisotropic compressions. *J. Chem. Phys.* **131**, 104504 (2009).
65. Nasikas, N. K., Edwards, T. G., Sen, S. & Papatheodorou, G. N. Structural characteristics of novel Ca–Mg orthosilicate and sub-orthosilicate glasses: Results from ²⁹Si and ¹⁷O NMR spectroscopy. *J. Phys. Chem. B* **116**(9), 2696–2702 (2012).
66. Schulte, A., Schirmacher, W., Schmid, B. & Unruh, T. Inelastic neutron and low-frequency Raman scattering in niobium-phosphate glasses: the role of spatially fluctuating elastic and elasto-optic constants. *J. Phys. Condens. Matter.* **23**, 213001 (2011).
67. Baldi, G. *et al.* Connection between boson peak and elastic properties in silicate glasses. *Phys. Rev. Lett.* **102**, 195502 (2009).
68. Mantis, B. *et al.* Non-Debye normalization of the glass vibrational density of states in mildly densified silicate glasses. *J. Phys. Condens. Matter* **22**, 025402 (2010).
69. Andrikopoulos, K. S., Christofilos, D., Kourouklis, G. A. & Yannopoulos, S. N. Pressure dependence of the Boson peak in glassy As₂S₃ studied by Raman scattering. *J. Non-Cryst. Solids.* **352**, 4594 (2006).
70. Carini, G. Jr., Carini, G., Cosio, D., D'Angelo, G. & Rossi, F. Low temperature heat capacity of permanently densified SiO₂ glasses. *Philos. Mag.* **96**(7–9), 761–773 (2016).
71. Elliott, S. R. A unified model for the low-energy vibrational behaviour of amorphous solids. *Europhys. Lett.* **19**, 201–206 (1992).
72. Duval, E., Boukenter, A. & Achibat, T. Vibrational dynamics and the structure of glasses. *J. Phys. Condens. Matter* **2**, 10227 (1990).
73. Schirmacher, W., Ruocco, G. & Scopigno, T. Acoustic attenuation in glasses and its relation with the boson peak. *Phys. Rev. Lett.* **98**, 025501 (2007).
74. Schirmacher, W. *et al.* Vibrational excitations in systems with correlated disorder. *Phys. Status Solidi C* **5**, 862–866 (2008).
75. Zhang, H. P., Fan, B. B., Wu, J. Q., Wang, W. H. & Li, M. Z. Universal relationship of boson peak with Debye level and Debye-Waller factor in disordered materials. *Phys. Rev. Mater.* **4**, 095603 (2020).
76. Tomoshige, N., Mizuno, H., Kim, K. & Matubayasi, N. Boson peak, elasticity, and glass transition temperature in polymer glasses: Effects of the rigidity of chain bending. *Sci. Rep.* **9**, 19514 (2019).
77. Monaco, A. *et al.* Effect of densification on the density of vibrational states of glasses. *Phys. Rev. Lett.* **97**, 135501 (2006).
78. Niss, K. *et al.* Influence of pressure on the boson peak: Stronger than elastic medium transformation. *Phys. Rev. Lett.* **99**, 055502 (2007).
79. Zanatta, M. *et al.* Elastic properties of permanently densified silica: A raman, brillouin light, and x-ray scattering study. *Phys. Rev. B* **81**, 212201 (2010).
80. Zanatta, M. *et al.* Debye to non-Debye scaling of the Boson peak dynamics: Critical behavior and local disorder in vitreous Germania. *J. Chem. Phys.* **135**, 174506 (2011).
81. Corezzi, S., Caponi, S., Rossi, F. & Fioretto, D. Stress-induced modification of the boson peak scaling behaviour. *J. Phys. Chem. B* **117**(46), 14477–14485 (2013).
82. Matsuda, Y. *et al.* Composition dependence of the boson peak and universality in lithium borate binary glasses: Inelastic neutron and raman scattering studies. *J. Phys. Soc. Jpn.* **79**, 033801 (2010).
83. Köhler, S., Ruocco, G. & Schirmacher, W. Coherent potential approximation for diffusion and wave propagation in topologically disordered systems. *Phys. Rev. B* **88**(6), 064203 (2013).
84. Yuan, F. & Huang, L. Brittle to ductile transition in densified silica glass. *Sci. Rep.* **4**, 5035 (2014).
85. Deschamps, T., Martinet, C., de Ligny, D., Bruneel, J. L. & Champagnon, B. Correlation between boson peak and anomalous elastic behavior in GeO₂ glass: An in situ Raman scattering study under high-pressure. *J. Chem. Phys.* **134**, 234503 (2011).
86. Fuhrmann, S., Deschamps, T., Champagnon, B. & Wondraczek, L. A reconstructive polyamorphous transition in borosilicate glass induced by irreversible compaction. *J. Chem. Phys.* **140**, 054501 (2014).

87. Carini, G. Jr., Carini, G., D'Angelo, G., Gilioli, E. & Vasi, C. Origin of excess low-energy vibrations in densified B₂O₃ glasses. *Philos. Mag.* **95**, 2596–2606 (2015).
88. Duval, E., Mermet, A. & Saviot, L. Vibrational dynamics and the structure of glasses. *Phys. Rev. B.* **75**, 024201 (2007).
89. Leonforte, F. Vibrational states and disorder in continuously compressed model glasses. *J. Non-Cryst. Solids.* **357**, 552–558 (2011).
90. Hehlen, B. & Simon, G. The vibrations of vitreous silica observed in hyper-Raman scattering. *J. Raman Spectrosc.* **43**, 1941–1950 (2012).
91. Shcheblanov, N. S., Povarnitsyn, M. E., Taraskin, S. N. & Elliott, S. R. Addendum and Erratum: Nature of vibrational excitations in vitreous silica. *Phys. Rev. B.* **94**, 903 (2016).
92. Shcheblanov, N. S. *et al.* Vibrational and structural properties of P2O5 glass: Advances from a combined modeling approach. *Phys. Rev. B.* **100**, 134309 (2019).

Acknowledgements

This project has received funding from the European Research Council (ERC) under the European Union's Horizon 2020 research and innovation program (Grant Number 681652).

Author contributions

L.W. designed the study. O.B. conducted vibrational spectroscopy. C.C. conducted NMR spectroscopy. M.B. and M.M.S. performed compaction experiments. Z.P., W.S. and L.W. implemented HET-CPA. Z.P. conducted data fits. Z.P. developed the reconstruction algorithm for spatial visualization. O.B., L.W. and C.C. wrote the first draft of the manuscript. All authors participated in data analysis and evaluation, and were involved in the discussion and manuscript revision.

Funding

Open Access funding enabled and organized by Projekt DEAL.

Competing interests

The authors declare no competing interests.

Additional information

Supplementary Information The online version contains supplementary material available at <https://doi.org/10.1038/s41598-021-04045-6>.

Correspondence and requests for materials should be addressed to L.W.

Reprints and permissions information is available at www.nature.com/reprints.

Publisher's note Springer Nature remains neutral with regard to jurisdictional claims in published maps and institutional affiliations.



Open Access This article is licensed under a Creative Commons Attribution 4.0 International License, which permits use, sharing, adaptation, distribution and reproduction in any medium or format, as long as you give appropriate credit to the original author(s) and the source, provide a link to the Creative Commons licence, and indicate if changes were made. The images or other third party material in this article are included in the article's Creative Commons licence, unless indicated otherwise in a credit line to the material. If material is not included in the article's Creative Commons licence and your intended use is not permitted by statutory regulation or exceeds the permitted use, you will need to obtain permission directly from the copyright holder. To view a copy of this licence, visit <http://creativecommons.org/licenses/by/4.0/>.

© The Author(s) 2021